High-Latitude Paleointensities During the Cretaceous Normal Superchron From the Okhotsk–Chukotka Volcanic Belt

E. M. Bobrovnikova[1], F. Lhuillier[2] , V. P. Shcherbakov[1] , V. V. Shcherbakova[1], G. V. Zhidkov[1], I. E. Lebedev[1], B. Eid[2] , and V. E. Pavlov[1,3]

[1]Schmidt Institute of Physics of the Earth, Russian Academy of Sciences, Moscow, Russia, [2]Department of Earth and Environmental Sciences,, Ludwig Maximilian University, Munich, Germany, [3]Department of Geology and Petroleum Technologies, Kazan Federal University, Kazan, Russia

Abstract We conducted an absolute paleointensity survey on 74 lava flows from the Okhotsk–Chukotka Volcanic Belt (NE Russia), emplaced 90–83 Ma toward the end of the Cretaceous Normal Superchron (CNS, 121–84 Ma). Relying on preliminary results, we restricted our analysis to eight lava flows (140 Thellier–Coe experiments), two of which also yielded successful Wilson determinations. A detailed analysis of the magneto-mineralogy—based on X-ray structural analysis, reflected-light microscopy, and thermomagnetic curves—indicates that the determinations from solely two lava flows can be fully trusted, with remanence carriers (a) dominated by low-titanium titanomagnetite, (b) showing unambiguous traces of high-temperature oxidation, and (c) yielding partial thermoremanent magnetization (pTRM) tails representative of pseudo-single-domain grains. Recalculated in terms of geomagnetic dipole strength, our two successful flow-mean determinations yield virtual dipole moments of $4.76 \pm 0.26 \times 10^{22}$ Am^2 ($N = 7$) and $9.07 \pm 0.84 \times 10^{22}$ Am^2 ($N = 8$). Using an updated version of the paleointensity database for the Cretaceous epoch, we stress that determinations based on nonglassy whole rocks, submarine basaltic glasses, and single crystals are mutually inconsistent, suggesting a separate analysis of their distributions is more appropriate. Despite statistically indistinguishable estimates of dipole strength before and after the onset of the CNS—in accord with recent studies refuting the existence of a strict correlation between chron duration and dipole moment—we found that the distribution of dipole moments during the CNS is slightly bimodal with a leptokurtic dominant mode, thus more inclined to produce outliers and suggesting distinct geomagnetic field behavior during the CNS.

Plain Language Summary The Cretaceous Normal Superchron (CNS, 121–84 Ma) is a salient feature of the geomagnetic field during the Phanerozoic, characterized by an anomalously long period of stable polarity whereas Earth's magnetic field stochastically reversed its polarity approximately 4 times per Myr during the last 5 million years. Deciphering the geomagnetic behavior during the CNS, in terms of average dipole strength and variability, is thus essential to better understand the *modus operandi* of the geodynamo and better constrain numerical models. To this end, we conducted absolute paleointensity (API) experiments on lava flows from the Okhotsk–Chukotka Volcanic Belt (NE Russia), yielding two estimates of the geomagnetic dipole strength toward the end of the CNS. Using an updated version of the API database, we show that average dipole strength is statistically indistinguishable before and after the onset of the CNS, suggesting the absence of a strict correlation between duration of polarity intervals and average dipole strength. In contrast, we also show that the distribution of dipole strength estimates is slightly bimodal, with the dominant mode being more peaked than a normal distribution. This feature may point to a higher propensity of the geodynamo to produce outliers and thus distinct geomagnetic behavior during the CNS.

1. Introduction

The geomagnetic field, generated by a dynamo process in Earth's fluid outer core, has experienced spatiotemporal changes over a wide range of timescales, which may have simultaneously or separately altered its geometry, polarity, variability, and average strength (e.g., Aubert et al., 2010). Over geological timescales, the geomagnetic field significantly varied its reversal frequency, from prolonged periods (>20 Myr) with stable polarity termed *superchrons* documented both during the Phanerozoic and the Proterozoic (e.g., Pavlov & Gallet, 2005, 2010) to episodes of hyperactivity with a reversal frequency greater than 10 Myr^{-1} documented in particular during the Jurassic, the Cambrian, and the late Ediacaran (e.g., Gallet & Pavlov, 2016). For the last 160 Myr, the geomagnetic polarity time scale (GPTS), mostly constrained by the analysis of sea-floor magnetic anomalies (e.g., Cande &

Kent, 1995; Channell et al., 1995), has often been divided into four linear segments lasting 30–40 Myr (Gallet & Hulot, 1997; Lowrie & Kent, 2004), yielding an average reversal frequency of 4.2 Myr^{-1} for 31–0 Ma, 1.3 Myr^{-1} for 74–31 Ma, nearly zero during the Cretaceous Normal Superchron (CNS, 121–84 Ma), 2.8 Myr^{-1} for 155–121 Ma (using the last version of the GPTS by Ogg, 2020). Such changes in the average reversal frequency have traditionally been linked to changes in the thermal boundary conditions at the core–mantle boundary (e.g., Biggin et al., 2012; Courtillot & Olson, 2007; Glatzmaier et al., 1999; McFadden & Merrill, 1984), although spontaneous nonlinear transitions of the geodynamo may also have played a significant role (e.g., Hulot & Gallet, 2003).

Over the past decades, the question of identifying a relationship between reversal frequency and geomagnetic dipole strength—quantified either in terms of virtual dipole moment (VDM) or virtual axial dipole moment (VADM) when paleoinclination is unknown—over the past 160 Myr has been highly debated (e.g., Biggin et al., 2008; Ingham et al., 2014; Kulakov et al., 2019; Tarduno et al., 2001). On the one hand, absolute paleo-intensity (API) determinations raised the hypothesis of a dipole low during the Mesozoic with a dipole strength 2–3 lower than the present-day one (e.g., Bol'shakov & Solodovnikov, 1981; Prévot et al., 1990; Shcherbakova et al., 2009, 2015; Tauxe et al., 2013) although this scenario has sometimes been challenged (e.g., Goguitchaichvili, 2002; Ruiz et al., 2006). On the other hand, API determinations raised the question of a dipole high during the CNS (e.g., Cottrell & Tarduno, 2000; Tarduno et al., 2001, 2002; Tauxe & Staudigel, 2004) although dipole moments similar to the present-day value have also repeatedly been obtained during this interval (e.g., Granot et al., 2007; Pick & Tauxe, 1993; Shcherbakova et al., 2012; Zhu et al., 2008). In a recent analysis of the PINT database (Biggin et al., 2010), Kulakov et al. (2019) argued in favor of an inverse correlation between reversal frequency and average dipole strength, as initially proposed by Cox (1968), whereas other studies failed to identify such a correlation at a sufficient confidence level (e.g., Ingham et al., 2014; Prévot et al., 1990; Selkin & Tauxe, 2000). The difficulty in answering this question can actually be ascribed to several factors: (a) the low-success rate and time-consuming nature of API experiments, (b) the unequal spatiotemporal distribution of API determinations, and (c) the complex identification of robust selection criteria to filter the API database.

To help answer this fundamental question of the relationship between reversal frequency and geomagnetic dipole strength, and thereby better constrain the *modus operandi* of the geodynamo, acquiring new API determinations during the CNS is a necessary task. To this end, we focus in this paper on the volcanic flows from the north-western part of the Okhotsk-Chukotka Volcanic Belt (OCVB), emplaced 90–84 Myr ago at a paleolatitude of ~81°N (Lebedev et al., 2021; Tikhomirov et al., 2021).

2. Settings and Methods

2.1. Geology and Sampling

The area of our research is located in the north-western part of Chukotka (NE Russia) on the border of the Anadyr and Central Chukotka segments of the OCVB (Figure 1a)—the largest marginal continental magmatic province extending for more than 3,000 km along the Pacific margin of Asia (e.g., Akinin & Miller, 2011; Tikhomirov et al., 2012). To the northeast of the Kupol gold deposit (66.9°N, 170.1°E), in the upper reaches of the Malyi Anyui River, we sampled 79 sites from seven distinct sections during two field campaigns in summers 2019 and 2020 (Lebedev et al., 2021; Tikhomirov et al., 2021). Each site was identified to be an independent basaltic flow with horizontal or subhorizontal occurrence (from 0° to 12°) of volcanogenic covers, usually controlled by paleorelief and elements of compensatory immersion structures. For each site, we collected 8–18 samples distributed on two or three different blocks to reduce within-flow variability. The samples, either obtained by drilling or hand probing, were then oriented with an inclinometer and a magnetic compass.

Age correlation between the sections is difficult due to the absence of reference horizons and significant lateral variability of volcanic complexes. However, the existing U–Pb and ^{40}Ar/^{39}Ar geochronology data indicate that the emplacement of the investigated sections within the Central Chukotka segment refers to a single pulse of volcanic activity that occurred 90–84 Myr ago (Tikhomirov et al., 2021). Zircons for U–Pb dating were selected from flows 0107 and 0117—the base and roof of section 01; flows 0400 and 0405—the base and middle of section 04 (Figure 1b; Tikhomirov et al., 2021). Therefore, in this paper, due to the complexity of interpolating the available ages, we computed a weighted average age of 87.02 ± 1.65 Ma based on the four U–Pb ages and valid for all studied flows in this area.
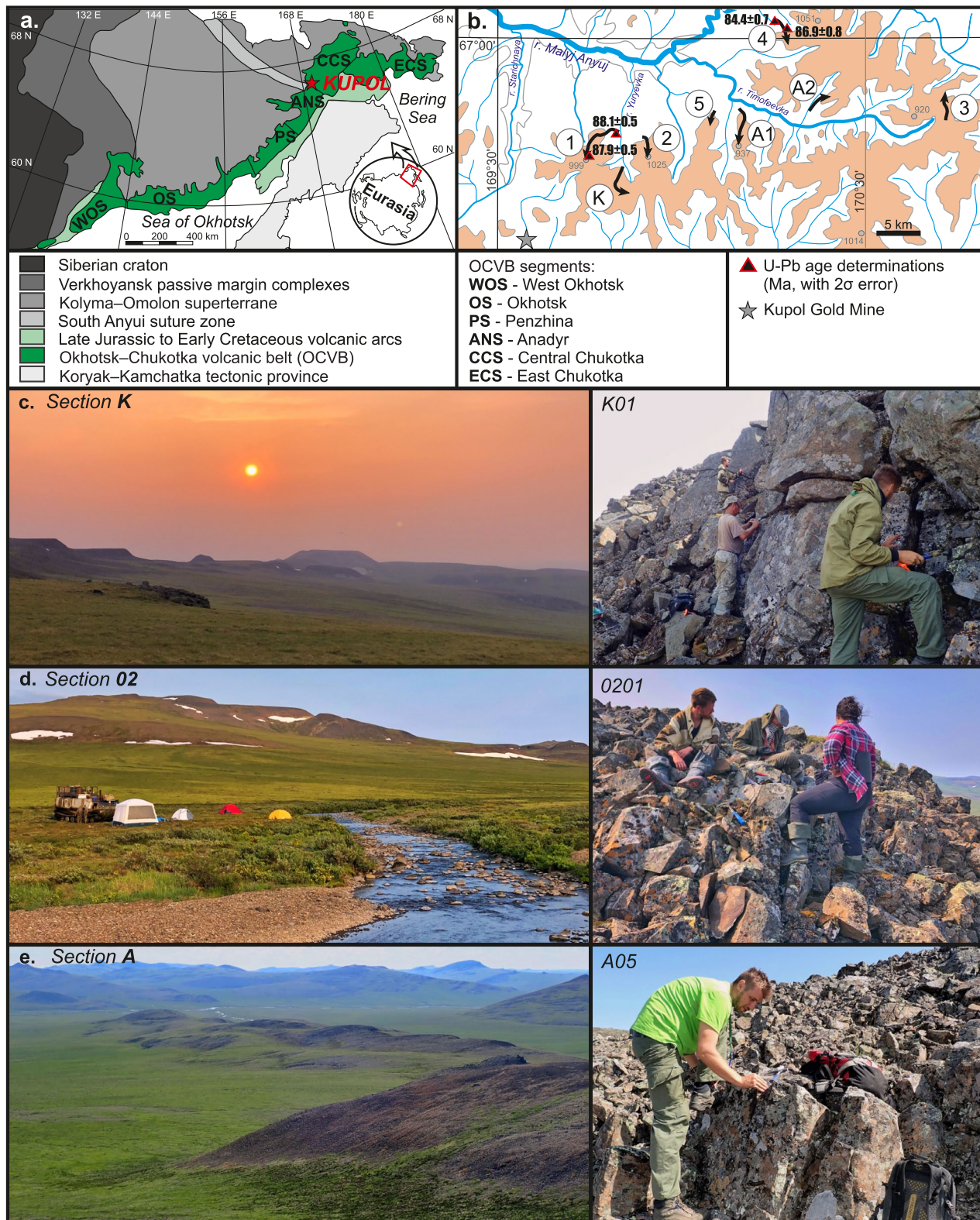
Figure 1. Geological settings. (a) Overview map of the Okhotsk–Chukotka Volcanic Belt (OCVB, NE Russia) emphasizing the key geological units. (b) Location of the seven investigated sections within the Central Chukotka segment. (c–e) Overview pictures of sections K, 02, and A with typical examples of lava flows in the right insets.

Paleomagnetic directions, successfully obtained for 74 out of 79 flows, indicate that the flows were emplaced in high polar latitudes (~81°N; Lebedev et al., 2021). Characteristic remanent magnetization (ChRM) was unambiguously determined by principal component analysis (Kirschvink, 1980) after the removal of a secondary component by heating to 150°C–200°C in most cases. These flows gave well-clustered directions (Figure 2a), yielding an unweighted Fisher-mean direction of $D = 4.7°$ and $I = 84.9°$ ($k = 44.8$, $\alpha_{95} = 2.5°$, $N = 74$), or a more robust Fisher-mean direction of $D = 6.8°$ and $I = 85.2°$ ($k = 40.8$, $\alpha_{95} = 3.0°$, $N = 55$) when averaging the serially correlated directions (Lebedev et al., 2021).

2.2. Magnetic Minerology

To select suitable lava flows for API determinations and assess the robustness of the conducted API experiments, rock-magnetic experiments, X-ray structural analysis, and observations by reflected-light microscopy were jointly conducted at the Institute of physics of the Earth (IPE) of the Russian Academy of Science (Moscow and Borok) and at the Ludwig Maximilian University (LMU) of Munich.

Hysteresis loops (corrected for paramagnetic contribution by the slope above 0.8 T) and backfield curves were obtained at IPE or LMU using a Lakeshore, one-component Vibrating Sample Magnetometer (VSM). From the saturation magnetization (M_S), remanent saturation magnetization (M_{RS}), coercive force (H_C), and remanent coercive force (H_{CR}), the ratios M_{RS}/M_S and H_{CR}/H_C were calculated to determine the hypothetical domain structure in the Day diagram (Day et al., 1977). The domain structure was also more robustly assessed on select samples by determining the amplitude of partial thermoremanent magnetization (pTRM) tails using at IPE, a custom-made, two-component VSM (Shcherbakova et al., 2000). To this end, the sample was first cooled down from T_C with a laboratory field B_{lab} switched on between T_1 and T_2 to impart the pTRM(T_1, T_2). The sample was then demagnetized until T_1 and cooled down in zero field to monitor the presence of a pTRM tail.

Continuous $M_S(T)$ curves were obtained by heating/cooling in air from room temperature to 600°C, using at IPE, a custom-made, one-component VSM in a laboratory field of 450 mT, or at LMU, a Variable Field Translation Balance (VFTB) in a laboratory field of 200 mT. The Curie points T_C of the ferrimagnetic phases were deduced by searching the minima of the first derivatives of the $M_S(T)$ curves (e.g., Fabian et al., 2013). To estimate the thermostability of magnetic minerals, cyclic $M_S(T)$ curves (to incrementally higher peak temperatures from 200°C to 600°C) were measured using at IPE, a custom-made Curie balance in a laboratory field of 450 mT, or at LMU, a VFTB in a laboratory field of 200 mT.

The magnetic fractions from 22 select samples were analyzed at IPE using a X-ray diffractometer STOE STADI MP (cobalt Kα_1 radiation). The diffraction spectra were first compared to the Crystallography Open Database (Gražulis et al., 2009, 2012) to identify the lattice constant a and the abundance of the titanomagnetite $Fe_{3-x}Ti_xO_4$ phases. The ulvöspinel content x and oxidation parameter z (fraction of original Fe^{2+} converted to Fe^{3+}) of each titanomagnetite phase were then estimated by comparing a and T_C with the empirical diagram by Nishitani and Kono (1983).

To further investigate the structure of the magnetic grains, 16 polished sections were observed at LMU using reflected-light microscopy. The sections, produced from 0.5 to 1 cm high slices, were first manually polished with silicon carbide foils (FEPA P180–P800 with average particle diameter from 80 to 20 μm) to flatten and smooth down the surface. They were then mechanically polished during 30–60 min with a 1 μm polycrystalline diamond paste, and 15 min with a ¼ μm polycrystalline diamond paste. The polished sections were observed with an oil objective mounted on a Leitz microscope with a final magnification varying from 250 to 1,500.

2.3. API Experiments

One part of the API experiments was conducted at IPE on 1-cm cubes, using an ORION three-component VSM (e.g., Shcherbakova et al., 2012, 2014, 2017), or a custom-made furnace together with an AGICO JR6 spinner magnetometer. The rest of the measurements were carried out at LMU on 8.8-mm or 1-in. diameter cores using an ASC-TD48 furnace together with an AGICO JR6 spinner magnetometer. No systematic trend was observed between the measurements made in the two laboratories.

Paleointensity determinations by the Thellier–Coe method (Coe, 1967; Thellier & Thellier, 1959), based on the stepwise replacement of a specimen's natural remanent magnetization (NRM) with pTRMs, were conducted in a
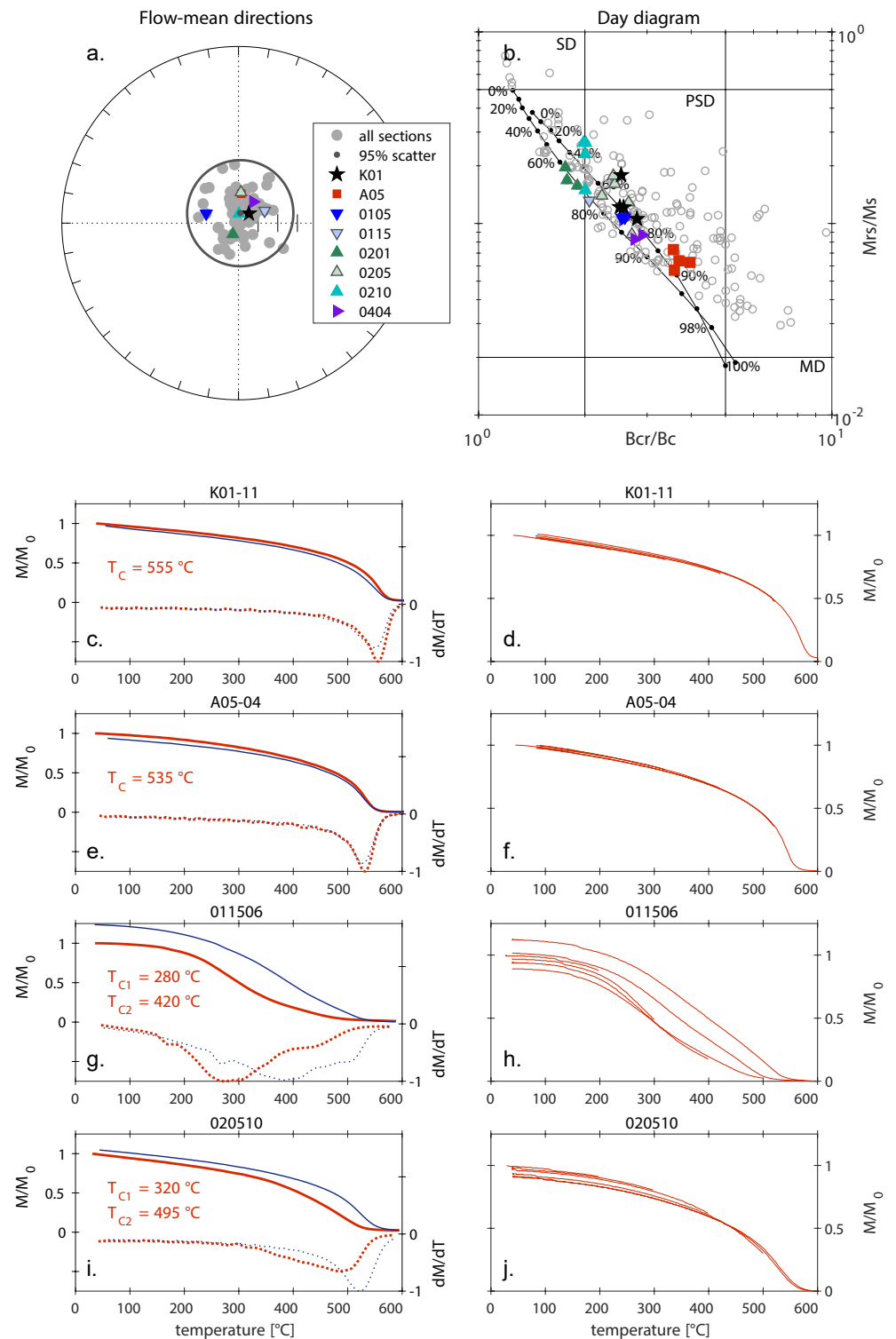
Figure 2. Paleomagnetic overview of the investigated lava flows. (a) Paleomagnetic directions obtained by Lebedev et al. (2021); (b) Day diagram with single-domain (SD)/multidomain (MD) mixing lines defined by Dunlop (2002). (c, e, g, i) Thermomagnetic curves $M_S(T)$ of the saturation magnetization up to 600°C showing heating (red bold lines) and cooling (blue thin lines) branches. The dashed lines represent the first derivative of the curves. (d, f, h, j) Cyclic $M_S(T)$ curves (to incrementally higher peak temperatures from 200°C to 600°C) to assess the thermostability of the samples.

laboratory field (B_{lab}) from 20 to 80 μT. Our experiments were performed for at least 12 temperature steps up to 500°C–630°C with pTRM checks to identify thermal alteration (Coe, 1967). Some experiments were also conducted with additional pTRM tail checks to assess the presence of nonideal remanence carriers (Riisager & Riisager, 2001). Each paleointensity was analyzed in an Arai–Nagata diagram (Nagata et al., 1963) by determining the best fit line over the selected temperature range while monitoring the NRM direction in a Zijderveld diagram (Zijderveld, 1967) and fitting the ChRM direction using principal component analysis (Kirschvink, 1980).

To assess the reliability of the Thellier–Coe determinations, we considered the PICRIT03 selection criteria (Kissel & Laj, 2004) as well as their modified version by Paterson et al. (2014). In the Arai–Nagata diagrams, these two sets of criteria require at least four points and three pTRM checks over the chosen temperature range; the NRM fraction used for the analysis, $f \geq 0.35$; the standard error of the slope normalized by its absolute value, $\beta \leq 0.1$; the quality factor (Coe et al., 1978), $q \geq 2$; the maximum difference ratio measured from pTRM checks (Selkin & Tauxe, 2000), DRAT <7% for PICRIT03 (10% for the modified version); and the absolute value of the sum of the pTRM differences (Kissel & Laj, 2004), CDRAT <10% (11% for the modified version). In the Zijderveld diagrams, the PICRIT03 selection criteria or their modified version require a mean angular deviation, MAD <7%, and the angular difference between ChRM directions for anchored and free-floating best fits of the directions, $\alpha < 15\%$.

The Wilson method (Wilson, 1961), known to be independent of domain state but only applicable to thermally stable samples (e.g., Muxworthy, 2010), was also applied on pilot samples for all sites, using an ORION, three-component VSM. In this technique, a specimen's continuous thermal demagnetization curve of the NRM is compared with that of a full TRM induced in a known B_{lab} varying from 20 to 40 μT in our case. The paleofield estimate B_{anc} corresponds to the slope in the NRM–TRM diagram over the chosen temperature interval. To assess the robustness of the determinations, we monitored the relative standard error (β) of the slope as well as the NRM fraction (f) and the normalized y-intercept (f_{res}).

Flow-mean paleointensity estimates were computed according to a hierarchical process. Paleointensities from multiple specimens at the sample level were first averaged while weighting the values by the inverse of the standard deviation. Paleointensities from multiple samples at the flow level were then averaged using the same weighting process.

2.4. World Paleointensity Database

We consider a subset of the World Paleointensity Database (WPD, maintained by the Borok Geophysical Observatory; Shcherbakov, Khokhlov, et al., 2019; Shcherbakov & Sycheva, 2006, 2013) for the Cretaceous period (145–66 Ma). This subset, available at https://doi.org/10.5282/ubm/data.263, encompasses all known published results in term of reconstructed dipole strength (VDM or VADM), including the most recent studies by Radhakrishna et al. (2020) and Di Chiara et al. (2021). This subset presently consists of 526 average estimates of dipole strength, predominantly determined using double-heating paleointensity protocols (330 for Thellier-style experiments, 13 for Wilson-style experiments) or less frequently using Shaw-style (102) or multispecimen (35) protocols. The paleointensities from this data set were obtained from various materials: nonglassy whole rocks (443), fragments from submarine basaltic glasses (76), or single crystals of plagioclase or zircon (19). In this paper, we only focus on paleointensity estimates obtained by the Thellier method with the mandatory presence of pTRM checks (version 01). We also required the following acceptance criteria: at least three individual paleointensity determinations per cooling unit with a relative standard error lower than 25% for the lenient version (version 02); at least five individual palaeointensity determinations per cooling unit with a relative standard error lower than 15% for the strict version (version 03).

3. Results

3.1. Rock-Magnetic Characterization

Among the 8 (out of 74) flows that will be scrutinized in Section 3.2, the bulk hysteresis properties shown in a Day diagram (Figure 2b) reveal that the majority of the samples belong to the area usually associated with pseudo-single-domain (PSD) behavior, distributed along the single-domain (SD)/multidomain (MD) mixing lines of magnetite defined by Dunlop (2002). Thermomagnetic curves indicate two distinct types of mineralogy for these

eight flows. On the one hand, flows K01, A05, and 0404 are characterized by a single ferrimagnetic phase with a Curie point T_C between 540°C and 570°C (Figures 2c and 2e) and high thermostability, to within a few percent, of the cyclic $M_S(T)$ curves up to 600°C (Figures 2d and 2f). On the other hand, flows 0105, 0115, 0201, 0205, and 0210 are characterized by a more heterogenous mineralogy with the coexistence of two ferrimagnetic phases: one low-temperature phase with T_C usually in the range 250°C–350°C; one higher-temperature phase with T_C usually in the range 400°C–500°C (Figures 2g and 2i). Samples with a dominant high-temperature T_C (e.g., flow 0205, Figure 2i) reveal thermostability, to within 10%, of the cyclic $M_S(T)$ curves up to 600°C. In contrast, samples with a dominant low-temperature T_C (e.g., flow 0115, Figure 2g) only reveal acceptable thermostability, to within 10%, of the cyclic $M_S(T)$ curves up to 400°C–500°C.

3.2. Paleointensity Results

Thellier experiments on 2–3 pilot samples from each of the 74 flows revealed that only eight flows (K01, A05, 0105, 0115, 0201, 0205, 0210, and 0404) were promising for further investigation. From these eight flows, we conducted a total of 140 Thellier experiments, among which 105 were interpreted (Table S1 in Supporting Information S1). For most samples, the ChRM component unambiguously trended to the origin after a secondary component was removed (Figure 3), consistent with the results from the directional analysis (Lebedev et al., 2021).

The Arai–Nagata diagrams from flow 0201 show a single slope fitted over 72%–92% (interquartile range) of the NRM fraction, the overprint component being removed by heating to 300°C–450°C (Table S1 in Supporting Information S1 and Figures 3a and 3b). We found for this flow a weak negative correlation between the minimum temperature and B_{anc}, suggesting a potential underestimation of B_{anc} by a few percent. In contrast, the diagrams from the other flows often yield two slopes over the interval of the ChRM component, the overprint component being removed by heating to 100°C–300°C (Figures 3c–3j). For these samples, the inflection of the curve was systematically observed around 400°C–500°C and followed by negative pTRM checks, suggesting that the high-temperature slope is likely the result of alteration during the experiment. The paleointensities were consequently fitted on the interval from 100°C–300°C to 400°C–500°C, over which the cyclic $M_S(T)$ curves did not record any obvious sign of thermal alteration (Figures 2d, 2f, 2h, and 2j). The negative pTRM tail checks on select samples from flows K01 and A05 (DRAT ≈ 5%, Figures 3c–3e) tend to rule out the presence of MD grains. Note, however, that this observation will be nuanced by the pTRM tail results presented in Section 3.3, indicating that flows A05, 0115, and 0210 are likely dominated by MD grains.

Wilson experiments on 2–3 pilot samples from each of the eight selected flows revealed that the Wilson method was only applicable to flows 0201 and 0210 (Table S2 in Supporting Information S1 and Figure 4). Most of the specimens show a single slope in the NRM–TRM diagram over the temperature interval of the ChRM component (Figures 4a, 4b, 4g, and 4h). Several samples from flow 0201 show a jump around 350°C–400°C on the TRM curve that may be the signature of a partial self-reversal (Figures 4c and 4d), possibly as a result of magnetostatic interactions between two distinct titanomagnetite phases (e.g., Krása et al., 2005). However, all specimens show an unambiguous unidirectional decay of the vector endpoints to the origin ($\alpha \leq 6°$, Table S2 in Supporting Information S1 and Figure 4). Paleointensities were fitted in most cases over a NRM fraction f higher than 50%, have a NRM residual fraction $f_{res} \leq 0.07$, and satisfy the selection rule $\beta \leq 0.02$ defined by Muxworthy (2010).

Figure 5 presents the individual API determinations for each of the eight considered lava flows. Among the 105 Thellier–Coe experiments that were interpreted (Table S1 in Supporting Information S1), 38 satisfy the PICRIT03 selection criteria (category A), 11 additional specimens satisfy the modified PICRIT03 selection criteria (category B), and 56 specimens do not satisfy any strict selection criteria (category C). Specimens from the latter category often fail to pass the directional selection criteria due to noisy Zijderveld diagrams but yield API estimates comparable to those from categories A and B. On the one hand, flows K01, 0115, 0201, 0210, and 0404 include at least three samples from category A or B, with weighted averages ranging from 28 ± 5.4 μT (flow 0210, $N = 8$, $\beta = 19\%$) to 68.8 ± 6.4 μT (flow K01, $N = 11$, $\beta = 9.3\%$). With the exception of flow 0115, we note that applying selection criteria leads to a reduction in the relative standard deviation β (Figure 5 and Table 1). We also note that Wilson and Thellier weighted averages from flows 0201 and 0210 yield indistinguishable values, to within errors (Figure 5 and Table 1). On the other hand, flows A05, 0105, and 0205 do not contain any Thellier determination satisfying the selection criteria and were consequently excluded from subsequent analysis (Figure 5 and Table 1).
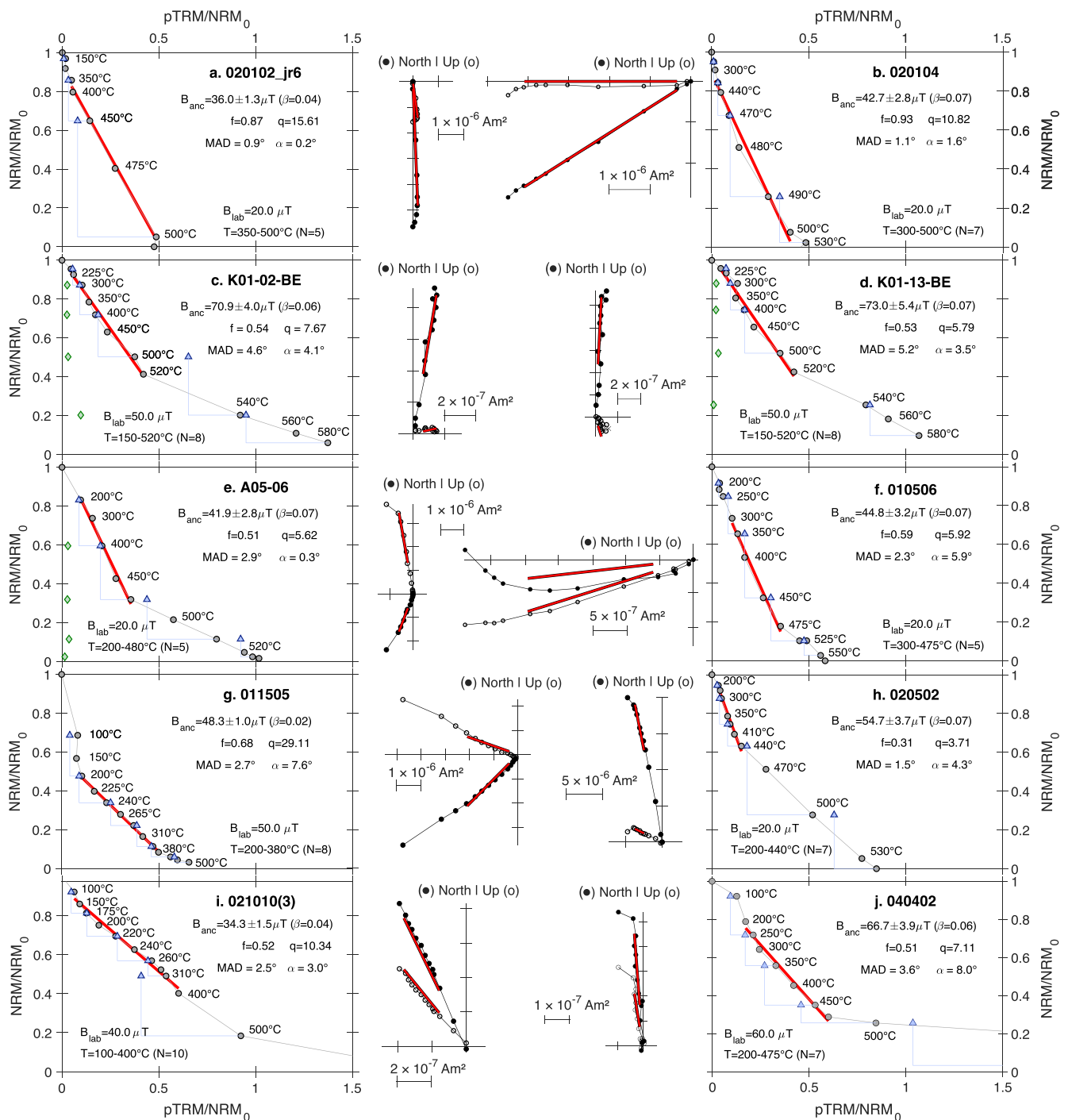
Figure 3. Typical absolute paleointensity results obtained from Thellier–Coe experiments for the eight investigated lava flows: Arai–Nagata diagrams with partial thermoremanent magnetization (pTRM) checks (blue triangles) and pTRM tail checks (green diamonds), supplemented with the Zijderveld diagrams of the natural remanent magnetization in specimen coordinates. Flows 0201 (a, b) and K01 (c, d) yield the most reliable paleointensity determinations, based on the analysis of the robustness of the remanence carriers (Section 3.3). See Section 2.3 for the definition of the parameters.

3.3. Description of the Remanence Carriers

Reflected-light microscopy, together with X-ray diffraction (XRD) structural analysis, indicates that the magnetic fraction of the investigated samples mainly consists of titanomagnetite grains of size ranging from 1 μm to several
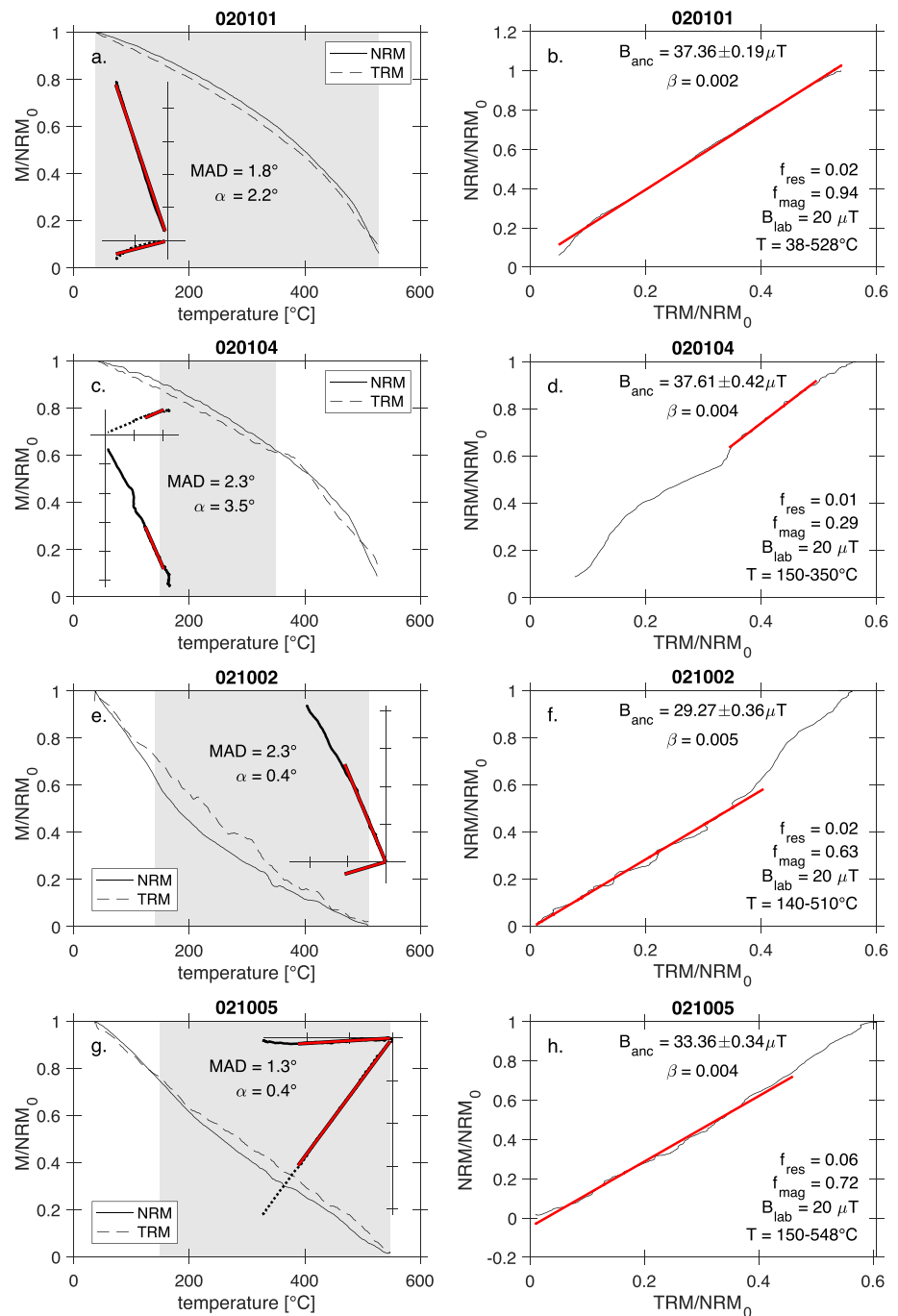
Figure 4. Typical absolute paleointensity results obtained from Wilson-style experiments for lava flows 0201 (a–d) and 0210 (e–h). Decay diagrams of the natural remanent magnetization (NRM) and laboratory-induced thermoremanent magnetization (TRM) on the left; Zijderveld diagrams of the NRM in the insets; and NRM–TRM diagrams on the right. See Section 2.3 for the definition of the parameters.

tens of μm. Due to the limited resolution of reflected-light microscopy, we focused our analysis on the structure of ~10 μm titanomagnetite grains.

In accordance with thermomagnetic curves, XRD structural analysis indicates that most samples are characterized by the coexistence of two titanomagnetite phases: one low-titanium phase with $x = 0.1$–0.3 and one
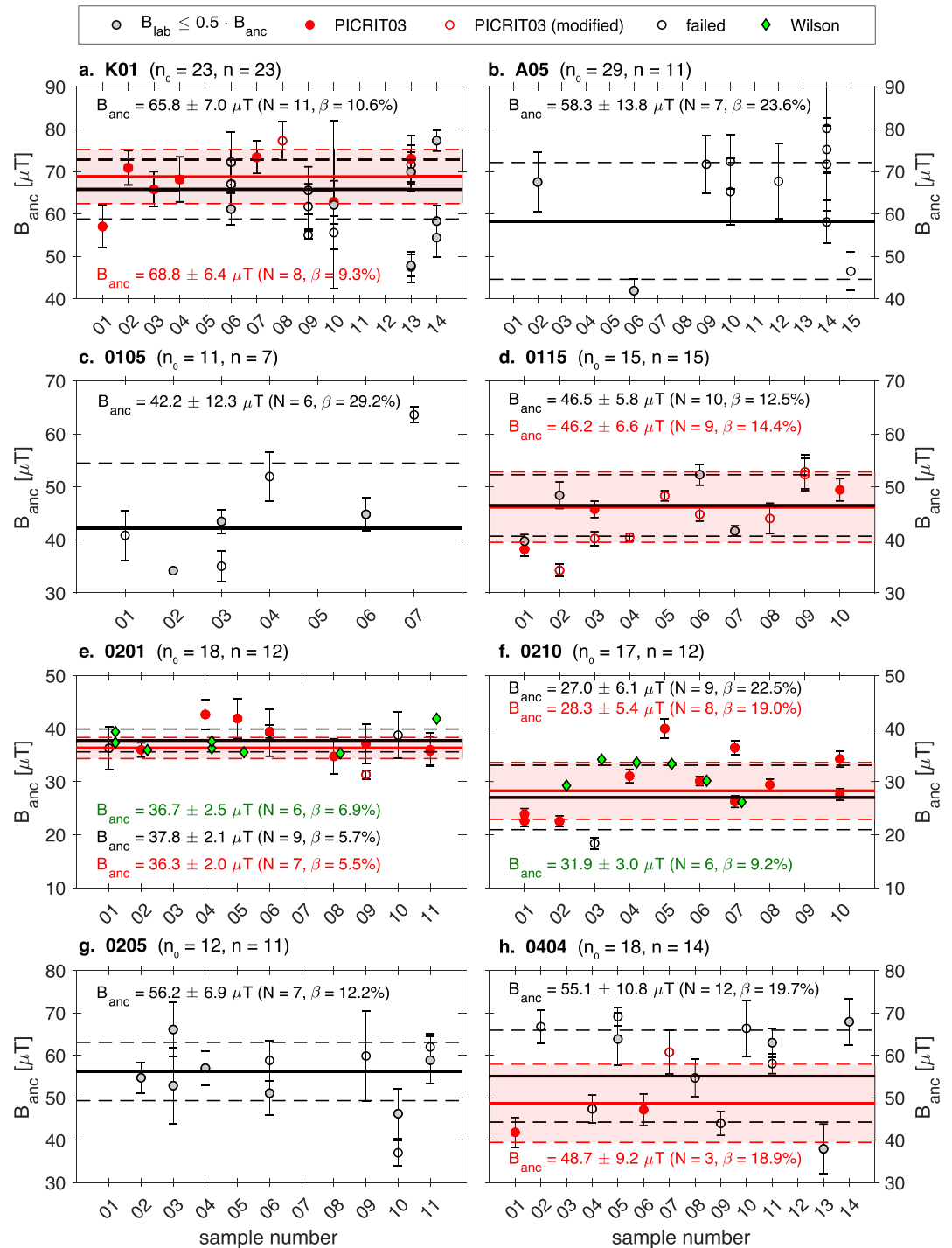
Figure 5. Individual absolute paleointensity results obtained from Thellier–Coe (circles) and Wilson (diamond) experiments for the eight investigated lava flows. The filled (resp. hollow) red circles correspond to the determinations that passed the PICRIT03 selection criteria (resp. their modified version by Paterson et al., 2014). The gray disks mark the rejected determinations conducted with a laboratory field more than 50% lower than the obtained paleointensity. For each flow, n_0 (resp. n) corresponds to the number of measured (resp. interpreted) specimens. Individual paleointensities were first averaged at the sample level to produce a flow-mean value B_{anc}, with N being the number of retained samples and β the relative standard deviation.

Table 1
Flow-Mean Absolute Paleointensity Results

Flow	Slon (°E)	Slat (°N)	N_{dir}	D (°)	I (°)	k	α_{95} (°)	Method	N_{int}	B_{anc} (μT)	$\sigma(B_{anc})$ (μT)	β (%)	VDM (10^{22} Am^2)	σ(VDM) (10^{22} Am^2)
K01	169.85	66.83	11 (14)	47.1	83.5	544	2	T	11 (11)	65.8	7	10.6	8.7	0.9
K01	**169.85**	**66.83**	**11 (14)**	**47.1**	**83.5**	**544**	**2**	**T***	**8 (11)**	**68.8**	**6.4**	**9.3**	**9.07**	**0.8**
A05	170.36	66.92	14 (15)	5.4	76.4	98.8	4	T	7 (16)	58.3	13.8	23.6	8.14	1.9
0105	169.77	66.89	7 (8)	286.6	74.5	108	5.8	T	6 (8)	42.2	12.3	29.2	6.0	1.8
0115	169.75	66.88	9 (10)	64.5	76.7	153.7	4.2	T	10 (10)	46.5	5.8	12.5	6.5	0.8
0115	169.75	66.88	9 (10)	64.5	76.7	153.7	4.2	T*	9 (10)	46.2	6.6	14.4	6.4	0.9
0201	169.88	66.89	10 (11)	207.2	84.3	290.8	2.8	T	9 (10)	37.8	2.1	5.7	5.0	0.3
0201	**169.88**	**66.89**	**10 (11)**	**207.2**	**84.3**	**290.8**	**2.8**	**T***	**7 (10)**	**36.3**	**2**	**5.5**	**4.8**	**0.3**
0201	169.88	66.89	10 (11)	207.2	84.3	290.8	2.8	W	6 (6)	36.7	2.5	6.9	4.8	0.3
0205	169.91	66.89	8 (11)	4.5	75.8	127.8	4.9	T	7 (8)	56.2	6.9	12.2	7.9	1.0
0210	169.92	66.88	10 (11)	2.8	85.7	248.9	3.1	T	9 (11)	27	6.1	22.5	3.5	0.8
0210	169.92	66.88	10 (11)	2.8	85.7	248.9	3.1	T*	8 (11)	28.3	5.4	19	3.7	0.7
0210	169.92	66.88	10 (11)	2.8	85.7	248.9	3.1	W	6 (6)	31.9	3	9.2	4.2	0.4
0404	170.29	67.00	13 (15)	34.5	78.1	158.7	3.3	T	12 (14)	55.1	10.8	19.7	7.6	1.5
0404	170.29	67.00	13 (15)	34.5	78.1	158.7	3.3	T*	3 (14)	48.7	9.2	18.9	6.7	1.3

Note. The quantities Slon and Slat report the longitude and latitude of the sites. The quantity N_{dir} reports the number of successful samples (analyzed samples, in parentheses) used to determine declination D, inclination I, Fisher's precision parameter k, and 95% confidence radius α_{95}. The next column reports the paleointensity method: T for Thellier–Coe before applying selection criteria, T* for Thellier–Coe after applying selection criteria, and W for Wilson. The quantity N_{int} reports the number of successful samples (analyzed samples, in parentheses) used to determine the paleofield B_{anc} with its standard deviation $\sigma(B_{anc})$ and relative standard error β. The abbreviation VDM stands for the virtual dipole moment reported with its standard deviation σ(VDM). In bold are the two most reliable flow-mean determinations retained after scrutinizing the robustness of the remanence carriers (Section 3.3).

higher-titanium phase with $x = 0.5$–0.8 (Table 2). The low-titanium phase is dominant for flows A05, K01, and 0404, with oxidation degree $z = 0.25$–0.50. At the other extreme, the high-titanium phase is ubiquitous for flow 0210, with oxidation degree $z = 0.43$. The other four flows show intermediate behavior, with the volume fraction of the low-titanium phase greater than 50% for flows 0201 and 0205, and the volume fraction of the high-titanium phase greater than 50% for flows 0105 and 0115.

Microphotographs from flows K01 (Figures 6a and 6b) and 0201 (Figure 6c) revealed the presence of ilmenite exsolution lamellae within most titanomagnetite grains, indicating that the samples were likely subjected to high-temperature oxidation. In contrast, microphotographs from flows 0105 (Figure 6d) and 0205 revealed the presence of microcracks on most titanomagnetite grains, indicating that the samples were likely subjected to low-temperature oxidation. Although less clearly evidenced by microscopic observations, flows A05, 0115, 0210, and 0404 may also have been subjected to low-temperature oxidation. The presence of the two distinct titanomagnetite phases is particularly visible for flows 0115 (Figure 6e) and 0404 (Figure 6f), with titanium-rich and titanium-poor areas being adjacent within one grain.

To better characterize the domain structure of the titanomagnetite grains, the continuous demagnetizations of pTRMs imparted on the temperature interval used for Thellier determinations revealed the existence of pTRM tails of amplitude lower than 10% for flows K01, 0105, 0201, and 0404 (Figures 7a, 7c, 7e, and 7f), suggesting the presence of PSD grains (Shcherbakova et al., 2000). In contrast, flows A05, 0115, 0210, and 0205 revealed the existence of pTRM tails of amplitude greater than 10%, arguing in favor of a MD behavior of the samples (Figures 7b, 7d, and 7f–7h). The discrepancy for sample A05–06 between the positive pTRM tail checks during the Thellier experiment (DRAT$_{tail}$ $\approx$ 5%, Figure 3e) and the presence of a tail of amplitude exceeding 15% during the pTRM tail experiment (Figure 7b) can be explained by the different experimental protocols. The pTRM tail experiments perform pTRM$_a(T_1,T_2)$ acquired by reaching the current Thellier temperature step T_1 from T_C, whereas the pTRM tail checks involve pTRM$_b(T_1,T_2)$ acquired by reaching T_1 from room temperature T_R. Knowing that the amplitude of pTRM$_a(T_1,T_2)$ tails—used as a reference to characterize the domain structure—usually

Table 2
Structural Analysis of Titanomagnetite Phases

Specimen	f_V	a (Å)	T_C (°C)	x	Z
A05-07	1.00	8.38	540	0.15	0.35
K01-06	0.15	8.44	320	0.50	0.28
	0.85	8.39	565	0.13	0.25
K01-06*	1.00	8.39	After heating to 525°C		
01-05-03	0.65	8.44	300	0.58	0.38
	0.35	8.41	495	0.23	0.18
01-15-02	0.62	8.44	290	0.55	0.30
	0.36	8.43	420	0.30	0.03
02-01-02	0.41	8.42	430	0.33	0.23
	0.59	8.41	520	0.18	0.13
02-01-02*	0.08	8.42	After heating to 500°C		
	0.82	8.39			
02-05-10	0.47	8.40	320	0.78	0.80
	0.53	8.38	490	0.33	0.55
02-10-07	1.00	8.44	240	0.68	0.43
04-04-11	0.93	8.39	540	0.15	0.28
	0.07	8.37	550	0.15	0.50

Note. The columns report the specimen name, the volume fraction f_V, the lattice constant a determined from X-ray diffractometry, and the Curie point determined from $M_S(T)$ experiments following the guidelines of Fabian et al. (2013). Ulvöspinel content x and oxidation parameter z were deduced from the Nishitani and Kono (1983)'s diagram for the unheated samples. The lattice constant of titanomagnetite $Fe_{3-x}Ti_xO_4$ ranges between 8.530 Å for ulvöspinel Fe_2TiO_4 and 8.397 Å for stoichiometric magnetite Fe_3O_4. To monitor chemical alteration, samples followed by an asterisk were remeasured after having been heated to 500°–525°C.

exceed those of $pTRM_b(T_1,T_2)$ tails (Shcherbakova et al., 2000), the pTRM tail checks are intrinsically prone to underestimate the amplitude of the tails and should thus be interpreted with caution (i.e., used to reject samples containing MD grains rather than to prove the presence of SD grains).

The small amplitude (6%–8%) of the pTRM tails for flows K01 and 0201—successfully passing the selection criteria in Section 3.2—confirms that the two-slope behavior in the Arai–Nagata diagrams cannot be ascribed to the presence of MD grains but rather to the occurrence of alteration during the experiments. This view is corroborated by XRD structural analysis conducted after heating the samples above the inflection temperature of 500°C–525°C observed in the Arai–Nagata diagrams. The high-titanium titanomagnetite phase is transformed into the already existing low-titanium titanomagnetite phase, indicating that the inflection in the Arai–Nagata diagram was probably caused by the thermally unstable high-titanium titanomagnetite phase.

Combining XRD structural analysis, reflected-light microscopy, and pTRM tail results, we reached the conclusion that only flows K01 and 0201—with 60%–85% of low-titanium titanomagnetite, clear traces of high-temperature oxidation, and pTRM tails lower than 10%—can be fully trusted for API determinations. We thus decided to exclude the other six flows from the subsequent analysis.

4. Discussion

4.1. Robustness of the API Experiments

We conducted an extensive set of API experiments on eight rapidly cooled lava flows from the north-western part of Chukotka (NE Russia). These flows were accurately dated by the U–Pb method on zircons from adjacent acidic flows (Tikhomirov et al., 2021). The weighted-mean age of 87.2 ± 1.65 Ma indicates that the investigated lava flows were emplaced at the termination of CNS (121–84 Ma; Ogg, 2020). These flows, with well-constrained paleodirections of normal polarity (Figure 2a), were emplaced at paleolatitude of 80.5° ± 4.9°N and are representative of a stable state of the geodynamo (Lebedev et al., 2021).

Except for flow 0201, Arai–Nagata diagrams often displayed two slopes—with an inflection observed around 400°C–500°C—and we decided to interpret the slope below 400°C–500°C. Whereas linear Arai–Nagata diagrams are predicted in the ideal case of assemblies of noninteracting SD grains bearing a TRM or a thermochemical remanent magnetization acquired by T_C increase (e.g., Shcherbakov, Gribov, et al., 2019; Shcherbakov et al., 2021), two-slope Arai–Nagata diagrams can be explained by multiple factors such as (a) the presence of two magnetization components, (b) the nonuniform magnetization in MD grains (e.g., Kosterov & Prévot, 1998; Levi, 1977), and (c) thermochemical alteration in natural conditions or in the course of laboratory experiments (e.g., Fabian, 2009; Zhao et al., 2014). For our samples, we argued that the alteration of a high-titanium titanomagnetite phase above 400°C–500°C is responsible for the shallower high-temperature slope.

The robustness of the Thellier API determinations was then assessed in a sequential way. We first submitted our results to the modified PICRIT03 selection criteria (Kissel & Laj, 2004; Paterson et al., 2014), leading to the rejection of three lava flows (A05, 0105, and 0205), a slight decrease in the within-flow dispersion for four flows (K01, 0201, 0210, and 0404), and a slight increase in the within-flow dispersion for one flow (0115). Four out of the five accepted flows satisfy the QPI STAT criterion (Biggin & Paterson, 2014; Paterson et al., 2010) with more than five independent API determinations. Among them, flows K01 and 0201 yield within-flow dispersion lower than 10% whereas flows 0115, 0210, and 0404 yield within-flow dispersion of 15%–20%. Independent of within-flow dispersion, flows 0201 and 0210 also yielded a successful set of Wilson API determinations, the weighted averages of which are indistinguishable from the Thellier determinations.
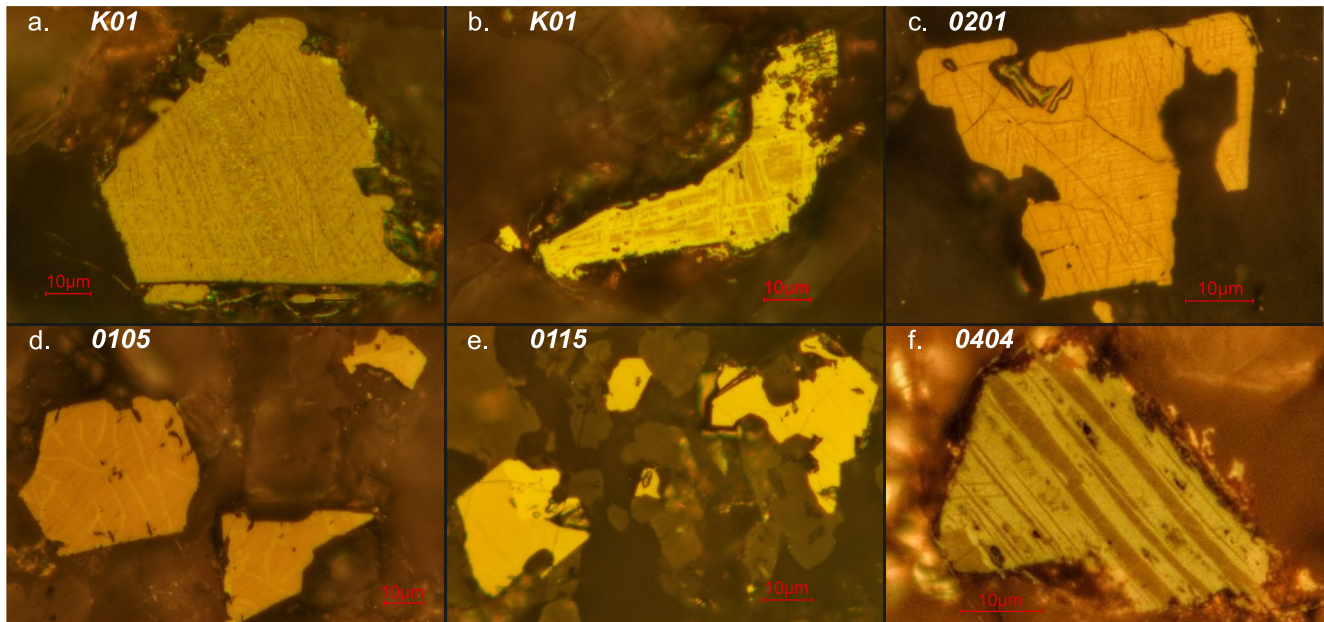
Figure 6. Typical microphotographs of titanomagnetite grains. (a–c) Ilmenite exsolution lamellae indicative of high-temperature oxidation for flows K01 and 0201. (d–e) Microcracks and/or presence of worm-like titanomaghemite suggestive of low-temperature oxidation for flows 0105 and 0115. (f) Example of the coexistence of two adjacent titanomagnetite phases within the same grain.

To better assess the reliability of the remanence carriers, both in terms of domain structure and pristine nature of the remanence, we conducted independent experiments (reflected-light microscopy, XRD structural analysis, and pTRM tail experiments). Strongest confidence was put on flows K01 and 0201, with unambiguous signs of high-temperature oxidation on predominantly low-titanium titanomagnetite grains (Figure 6 and Table 2). In terms of domain structure, flows K01 and 0201 also proved to have pTRM tails lower than 8% (Figure 7), ruling out the presence of MD remanence carriers and confirming that the two-slope nature of the Arai–Nagata diagrams should be ascribed to alteration during the experiments rather than MD effect. Alternatively, this nonideal behavior could also be explained by irreversible changes in the domain state of the ferrimagnetic grains within the PSD range (e.g., Tanaka & Yamamoto, 2016). The remaining other two flows (0115 and 0210) satisfying the QPI STAT criterion suffer from a twofold weakness—possible traces of low-temperature oxidation on the one hand, obvious signs of MD behavior on the other—suggesting their rejection of the paleointensity data set.

We therefore conclude that only flows K01 and 0201 can be deemed robust for API determinations, yielding a success rate of 2%–3% (2 successful out of the 74 originally investigated lava flows) consistent with paleointensity surveys on volcanic rocks (e.g., Tauxe & Yamazaki, 2015; Valet, 2003). For the present collection of API determinations, the technical selection criteria evaluating the robustness of the Arai–Nagata and Zijderveld diagrams are necessary but not sufficient to exclude all unreliable lava flows. The QPI STAT criterion (Biggin & Paterson, 2014; Paterson et al., 2010) and the mutual agreement between Thellier and Wilson API determinations are also insufficient in our case to improve the selection process. These examples illustrate the difficulty in finding universal technical selection criteria (e.g., Jeong et al., 2021; Paterson et al., 2014, 2015) and indicate that, whenever possible, a careful analysis of the robustness of the remanence carriers should be conducted before including new results into the API database (e.g., Lhuillier et al., 2017, 2019).

4.2. Dipole Strength Behavior During the CNS

Recalculated in terms of geomagnetic dipole strength, our two successful flow-mean API determinations yield VDM values of $9.07 \pm 0.84 \times 10^{22}$ Am^2 ($N = 8$) for flow K01 and $4.76 \pm 0.26 \times 10^{22}$ Am^2 ($N = 7$) for flow 0201 (Table 1). Given that the two lava flows are likely to describe time-independent snapshots of the geomagnetic field over an interval of a few Myr at the termination of the CNS, a twofold variation of the dipole moment is
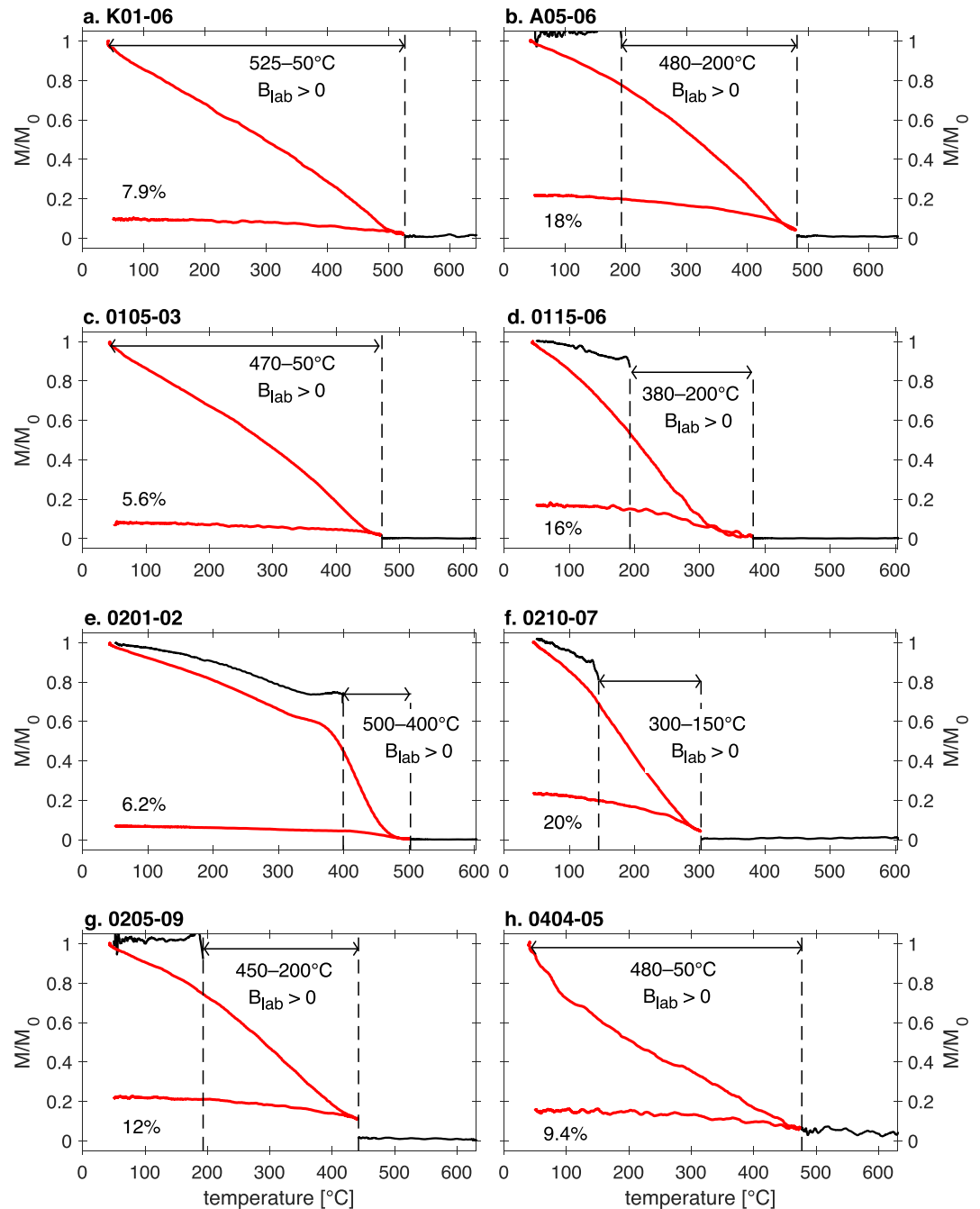
Figure 7. Examples of pTRM tail experiments for the eight investigated flows. Samples were first imparted a pTRM (T_1, T_2) by cooling down from T_C. Samples were then continuously demagnetized until T_1 and cooled down in zero field to monitor the presence of a pTRM tail. The temperature range (T_1, T_2) corresponds to the temperature of the best fit line in the Arai–Nagata diagram. Only flows K01, 0105, and 0201 show a behavior consistent with pseudo-single-domain (PSD) grains (pTRM tail ≤ 10%), whereas the other flows are probably dominated by multidomain (MD) grains.

plausible when compared to the rate of change of the dipole moment over the past 2 Myr (e.g., Valet et al., 2005; Ziegler et al., 2011).

To investigate the behavior of the dipole strength during the CNS, we considered various versions of the WPD database for Thellier-style determinations with pTRM checks, looking in particular at the discrepancies between paleointensities obtained from different materials (Figure 8). In the unfiltered version of the database (version
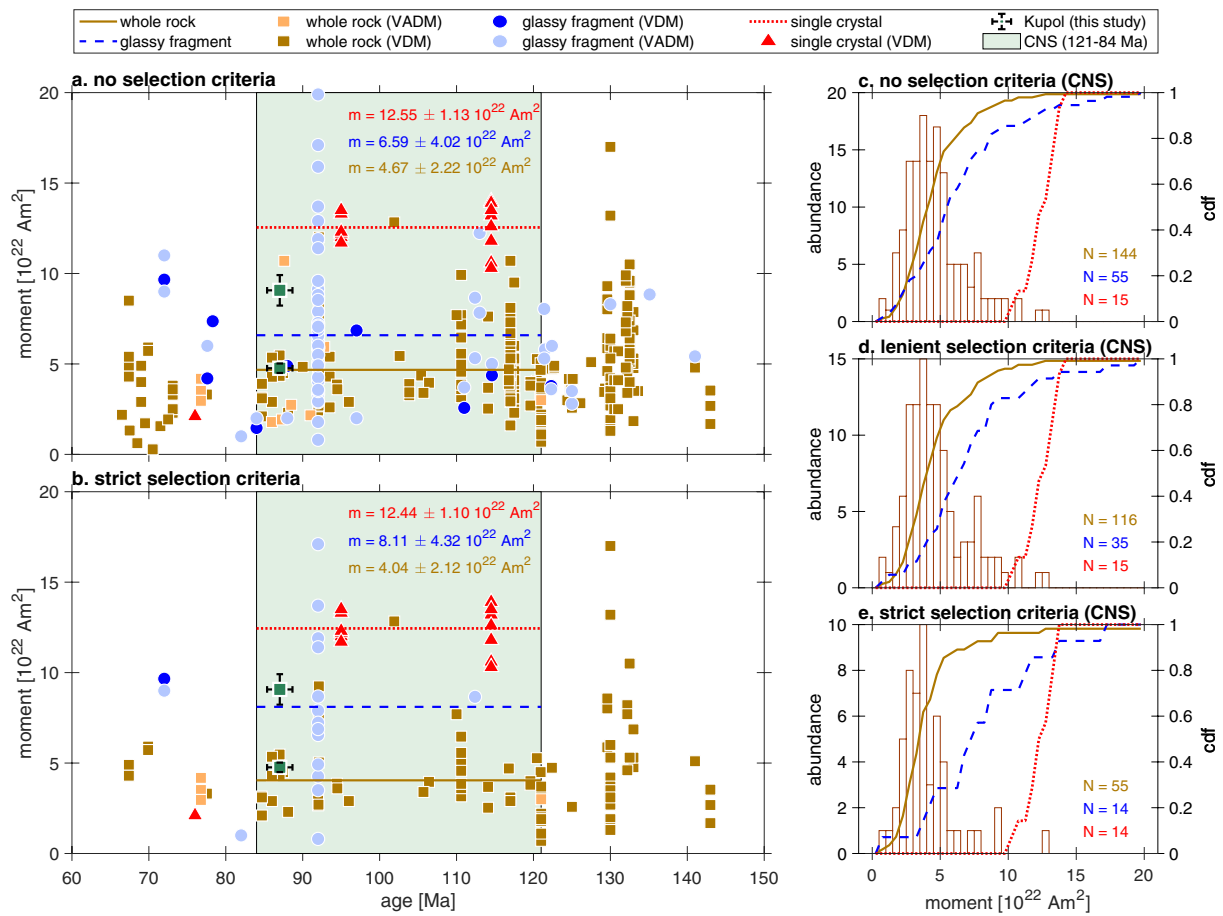
Figure 8. Analysis of the absolute paleointensity (API) database for the Cretaceous period. (a–b) Dipole moment (virtual dipole moment [VDM] or virtual axial dipole moment [VADM]) as a function of age. (c–e) Histogram and cumulative density function (cdf) of dipole moments during the Cretaceous Normal Superchron (CNS, 121–84 Ma). In all panels, we only considered dipole moments obtained from Thellier-style experiments with pTRM checks: in the absence of selection (panels a and c), with lenient selection criteria (at least three individual determinations per cooling unit with relative standard deviation ≤15%, panel d), or with strict selection criteria (at least five individual determinations per cooling unit with relative standard deviation ≤25%, panels b and e). Three types of material are considered: nonglassy whole rocks (brown squares, solid line), glassy fragments (blue circles, dashed line), and single crystals (red triangles, dotted line).

1, Figures 8a and 8c), it appears that the three subsets obtained from nonglassy whole rocks (mostly basalts), glassy fragments (mostly submarine volcanic glasses, e.g., Di Chiara et al., 2021; Tauxe, 2006; Tauxe & Staudigel, 2004), and single crystals (e.g., Tarduno et al., 2001, 2002) yield inconsistent results. The average dipole moment during the CNS from single crystals ($m = 12.55 \pm 1.13 \times 10^{22}$ Am^2, $N = 15$) is indeed twice as large as the average value from nonglassy whole rocks ($m = 4.69 \pm 2.22 \times 10^{22}$ Am^2, $N = 143$), whereas the average value from glassy fragments lies in between ($m = 6.52 \pm 4.02 \times 10^{22}$ Am^2, $N = 59$). In a more quantitative way, two-sample t-tests between each pair of subsets systematically lead to the rejection (p-value $\leq 10^{-5}$) of the null hypothesis according to which the two subsets would be drawn from the same normal distribution. Such a result is reproduced when using the second (Figure 8d, lenient selection criteria, $N \geq 3$ and $\beta \leq 25\%$) and third (Figures 8b and 8e, strict selection criteria, $N \geq 5$ and $\beta \leq 15\%$) versions of the database, confirming that, in the current state of the database, the three subsets are unlikely to be drawn from the same normal distribution. Whether such a discrepancy is the result of insufficient spatiotemporal sampling or of an intrinsic bias between the different materials remains an open question (e.g., Kulakov et al., 2019). At any rate, it indicates that, in the current state of the database, the three subsets should be considered separately to analyze the distribution of the dipole moments during the CNS. As the subsets from glassy fragments and single crystals are too sparse for a robust statistical analysis, we focus the rest of the discussion on nonglassy whole rocks only.

Whatever the chosen filtering version, the distribution of dipole moments is statistically distinct from a normal distribution (rejection of the null hypothesis of a Kolmogorov–Smirnov test with a p-value $\leq 10^{-40}$). In the

absence of selection (version 1, $N = 144$), the distribution is right tailed with a skewness of 1.11. In the case of lenient selection criteria (version 2, $N = 116$), the distribution shows similar behavior in terms of asymmetry (skewness of 1.13) but with more pronounced bimodality, which may be the signature of distinct geomagnetic behavior during the CNS (e.g., Shcherbakova et al., 2012) and would be consistent with a bistable geodynamo during the CNS (e.g., Lhuillier et al., 2016). In the case of strict selection criteria (version 3, $N = 55$), this feature becomes however less obvious, unless the nondominant mode is represented by the three points with $m \geq 9 \times 10^{22}$ Am^2 based on two determinations on gabbro (Granot et al., 2007; Tsunakawa et al., 2009) and our determination from basaltic flow K01. Considering the dominant mode (i.e., discarding these three previous points), we get an excess kurtosis of 3.7, more consistent with a Laplace distribution (excess kurtosis of 3) than a normal distribution (excess kurtosis of 0). On the one hand, a leptokurtic (i.e., with an excess kurtosis greater than three) distribution could be the result of the mixture of normal distributions (e.g., Khokhlov & Hulot, 2017; Khokhlov et al., 2017) and thus reflecting more complex geomagnetic behavior than the one observed during the past 3 Myr—characterized by a nearly normal distribution and less inclined to produce outliers (e.g., Lhuillier et al., 2017). On the other hand, caution must be exercised as the distribution only relies on 55 points that, despite the strict selection criteria, can still be contaminated by errors (e.g., Smirnov et al., 2017). For this restricted data set, we note that the hypothetical bimodality of the distribution cannot be explained by a dependency of the dipole moments on paleolatitude, the values with inclination $\geq 45°$ being statistically indistinguishable from the values with inclination $< 45°$ (Kolmogorov–Smirnov test, p-value of 1).

Using the strictest selection criteria, we obtain average estimates of dipole moment before the CNS (144–121 Ma, $m = 5.29 \pm 3.53 \times 10^{22}$ Am^2, $N = 31$) and after the CNS (81–66 Ma, $m = 4.19 \pm 1.12 \times 10^{22}$ Am^2, $N = 9$) that are both seemingly higher than the one during the CNS (121–84 Ma, $m = 4.04 \pm 2.12 \times 10^{22}$ Am^2, $N = 55$). Nevertheless, a more robust comparison using two-sample Kolmogorov–Smirnov tests indicate that, at the 5% significance level, one cannot reject the null hypothesis according to which the three subsets are drawn from the same continuous distribution. We thus conclude that, for the present version of the database analyzed during the Cretaceous period, the strength of the geomagnetic field, based on API determinations on nonglassy whole rocks, is not significantly different before and after the onset of the CNS, consistent with the recent analysis by Di Chiara et al. (2021) on submarine basaltic glasses and tending to argue against a strict correlation between chron duration and dipole moment.

5. Conclusions

Using strict selection criteria combined with a careful analysis of the remanence carriers, we determined two robust paleointensity estimates at the end of the CNS before analyzing the distribution of geomagnetic dipole moments during the CNS. Based on an updated version of the API database, we emphasize that

1. determinations based on nonglassy whole rocks, submarine basaltic glasses, and single crystals are mutually incompatible, in accord with previous observations (e.g., Kulakov et al., 2019) suggesting a separate analysis of their distributions;
2. dipole strength estimates over the Cretaceous time window (145–66 Ma) are statistically indistinguishable before and after the onset of the CNS, in accord with recent studies (e.g., Di Chiara et al., 2021) refuting a strict correlation between chron duration and dipole moment; and
3. the distribution of dipole moments during the CNS may be bimodal, in accord with previous observations (e.g., Shcherbakova et al., 2012) suggesting possible distinct geomagnetic behavior during the CNS (e.g., Lhuillier et al., 2016).

Data Availability Statement

Specimen-level paleointensity data as well as the updated version of the World Paleointensity Database (WPD) are available at https://doi.org/10.5282/ubm/data.263.

References

Akinin, V. V., & Miller, E. L. (2011). Evolution of calc-alkaline magmas of the Okhotsk–Chukotka Volcanic Belt. *Petrology*, *19*(3), 237–277. https://doi.org/10.1134/S0869591111020020

Aubert, J., Tarduno, J. A., & Johnson, C. L. (2010). Observations and models of the long-term evolution of Earth's magnetic field. *Space Science Reviews*, *155*, 337–370. https://doi.org/10.1007/s11214-010-9684-5

Biggin, A. J., McCormack, A., & Roberts, A. P. (2010). Paleointensity database updated and upgraded. *Eos*, *91*(2), 15. https://doi.org/10.1029/2010EO020003

Biggin, A. J., & Paterson, G. A. (2014). A new set of qualitative reliability criteria to aid inferences on palaeomagnetic dipole moment variations through geological time. *Frontiers in Earth Science*, *2*, 1–9. https://doi.org/10.3389/feart.2014.00024

Biggin, A. J., Steinberger, B., Aubert, J., Suttie, N., Holme, R., & Torsvik, T. H. (2012). Possible links between long-term geomagnetic variations and whole-mantle convection processes. *Nature Geoscience*, *5*(8), 526–533. https://doi.org/10.1038/ngeo1521

Biggin, A. J., van Hinsbergen, D. J. J., Langereis, C. G., Straathof, G. B., & Deenen, M. H. L. (2008). Geomagnetic secular variation in the Cretaceous Normal Superchron and in the Jurassic. *Physics of the Earth and Planetary Interiors*, *169*, 3–19. https://doi.org/10.1016/j.pepi.2008.07.004

Bol'shakov, A. S., & Solodovnikov, G. M. (1981). Geomagnetic field intensity in last 400 million year. *Doklady Akademii Nauk SSSR*, *260*(6), 1340–1343.

Cande, S., & Kent, D. V. (1995). Revised calibration of the geomagnetic polarity timescale for Late Cretaceous and Cenozoic. *Journal of Geophysical Research*, *100*(B4), 6093–6095. https://doi.org/10.1029/94JB03098

Channell, J. E. T., Erba, E., Nakanishi, M., & Tamaki, K. (1995). Late Jurassic–Early Cretaceous time scales and oceanic magnetic anomaly block models. In W. A. Berggren, D. V. Kent, M.-P. Aubry, & J. Hardenbol (Eds.), *Geochronology, time scales and global stratigraphic correlation* (Vol. 54, pp. 51–63). SEPM. https://doi.org/10.2110/pec.95.04.0051

Coe, R. S. (1967). The determination of paleo-intensities of the Earth's magnetic field with emphasis on mechanisms which could cause non-ideal behavior in Thellier's method. *Journal of Geomagnetism and Geoelectricity*, *19*(3), 157–179. https://doi.org/10.5636/jgg.19.157

Coe, R. S., Grommé, C. S., & Mankinen, E. A. (1978). Geomagnetic paleointensities from radiocarbon-dated lava flows on Hawaii and the question of the Pacific nondipole low. *Journal of Geophysical Research*, *83*(B4), 1740–1756. https://doi.org/10.1029/JB083iB04p01740

Cottrell, R. D., & Tarduno, J. A. (2000). In search of high-fidelity geomagnetic paleointensities: A comparison of single plagioclase crystal and whole rock Thellier–Thellier analyses. *Journal of Geophysical Research*, *105*(B10), 23579–23594. https://doi.org/10.1029/2000JB900219

Courtillot, V., & Olson, P. L. (2007). Mantle plumes link magnetic superchrons to Phanerozoic mass depletion events. *Earth and Planetary Science Letters*, *260*, 495–504. https://doi.org/10.1016/j.epsl.2007.06.003

Cox, A. V. (1968). Lengths of geomagnetic polarity intervals. *Journal of Geophysical Research*, *73*(10), 3247–3260. https://doi.org/10.1029/JB073i010p03247

Day, R., Fuller, M. D., & Schmidt, V. A. (1977). Hysteresis properties of titanomagnetites: Grain-size and compositional dependence. *Physics of the Earth and Planetary Interiors*, *13*(4), 260–267. https://doi.org/10.1016/0031-9201(77)90108-X

Di Chiara, A., Tauxe, L., Staudigel, H., Florindo, F., Protti, M., Yu, Y., et al. (2021). Earth's magnetic field strength and the Cretaceous Normal Superchron: New data from Costa Rica. *Geochemistry, Geophysics, Geosystems*, *22*(4), e2020GC009605. https://doi.org/10.1029/2020GC009605

Dunlop, D. J. (2002). Theory and application of the Day plot (M_{rs}/M_s versus H_{cr}/H_c) 1. Theoretical curves and tests using titanomagnetite data. *Journal of Geophysical Research*, *107*(B3), 2056. https://doi.org/10.1029/2001JB000486

Fabian, K. (2009). Thermochemical remanence acquisition in single-domain particle ensembles: A case for possible overestimation of the geomagnetic paleointensity. *Geochemistry, Geophysics, Geosystems*, *10*, Q06Z03. https://doi.org/10.1029/2009GC002420

Fabian, K., Shcherbakov, V. P., & McEnroe, S. A. (2013). Measuring the Curie temperature. *Geochemistry, Geophysics, Geosystems*, *14*, 947–961. https://doi.org/10.1029/2012GC004440

Gallet, Y., & Hulot, G. (1997). Stationary and nonstationary behaviour within the geomagnetic polarity time scale. *Geophysical Research Letters*, *24*(15), 1875–1878. https://doi.org/10.1029/97GL01819

Gallet, Y., & Pavlov, V. E. (2016). Three distinct reversing modes in the geodynamo. *Izvestiya, Physics of the Solid Earth*, *52*(2), 291–296. https://doi.org/10.1134/S106935131602004X

Glatzmaier, G. A., Coe, R. S., Hongre, L., & Roberts, P. H. (1999). The role of the Earth's mantle in controlling the frequency of geomagnetic reversals. *Nature*, *401*(6756), 885–890. https://doi.org/10.1038/44776

Goguitchaichvili, A. (2002). On the reliability of Mesozoic Dipole Low: New absolute paleointensity results from Paraná Flood Basalts (Brazil). *Geophysical Research Letters*, *29*(13), 1655. https://doi.org/10.1029/2002GL015242

Granot, R., Tauxe, L., Gee, J. S., & Ron, H. (2007). A view into the Cretaceous geomagnetic field from analysis of gabbros and submarine glasses. *Earth and Planetary Science Letters*, *256*, 1–11. https://doi.org/10.1016/j.epsl.2006.12.028

Gražulis, S., Chateigner, D., Downs, R. T., Yokochi, A. F. T., Quirós, M., Lutterotti, L., et al. (2009). Crystallography Open Database—An open-access collection of crystal structures. *Journal of Applied Crystallography*, *42*(4), 726–729. https://doi.org/10.1107/S0021889809016690

Gražulis, S., Daškevič, A., Merkys, A., Chateigner, D., Lutterotti, L., Quirós, M., et al. (2012). Crystallography Open Database (COD): An open-access collection of crystal structures and platform for world-wide collaboration. *Nucleic Acids Research*, *40*(D1), 420–427. https://doi.org/10.1093/nar/gkr900

Hulot, G., & Gallet, Y. (2003). Do superchrons occur without any palaeomagnetic warning? *Earth and Planetary Science Letters*, *210*, 191–201. https://doi.org/10.1016/S0012-821X(03)00130-4

Ingham, E., Heslop, D., Roberts, A. P., Hawkins, R., & Sambridge, M. (2014). Is there a link between geomagnetic reversal frequency and paleointensity? A Bayesian approach. *Journal of Geophysical Research: Solid Earth*, *119*, 5290–5304. https://doi.org/10.1002/2014JB010947

Jeong, D., Liu, Q., Yamamoto, Y., Yu, Y., Zhao, X., & Qin, H. (2021). New criteria for selecting reliable Thellier-type paleointensity results from the 1960 Kilauea lava flows, Hawaii. *Earth, Planets and Space*, *73*, 144. https://doi.org/10.1186/s40623-021-01473-6

Khokhlov, A. V., & Hulot, G. (2017). On the cause of the non-Gaussian distribution of residuals in geomagnetism. *Geophysical Journal International*, *209*, 1036–1047. https://doi.org/10.1093/gji/ggx071

Khokhlov, A. V., Lhuillier, F., & Shcherbakov, V. P. (2017). Intermittence and peculiarities of a statistic characteristic of the geomagnetic field in geodynamo models. *Izvestiya, Physics of the Solid Earth*, *53*(5), 695–701. https://doi.org/10.1134/S106935131705007X

Kirschvink, J. L. (1980). The least-squares line and plane and the analysis of palaeomagnetic data. *Geophysical Journal of the Royal Astronomical Society*, *62*(3), 699–718. https://doi.org/10.1111/j.1365-246X.1980.tb02601.x

Kissel, C., & Laj, C. (2004). Improvements in procedure and paleointensity selection criteria (PICRIT-03) for Thellier and Thellier determinations: Application to Hawaiian basaltic long cores. *Physics of the Earth and Planetary Interiors*, *147*(2–3), 155–169. https://doi.org/10.1016/j.pepi.2004.06.010

Kosterov, A. A., & Prévot, M. (1998). Possible mechanisms causing failure of Thellier palaeointensity experiments in some basalts. *Geophysical Journal International*, *134*, 554–572. https://doi.org/10.1046/j.1365-246x.1998.00581.x

Krása, D., Shcherbakov, V. P., Kunzmann, T., & Petersen, N. (2005). Self-reversal of remanent magnetization in basalts due to partially oxidized titanomagnetites. *Geophysical Journal International*, *162*, 115–136. https://doi.org/10.1111/j.1365-246X.2005.02656.x

Kulakov, E. V., Sprain, C. J., Doubrovine, P. V., Smirnov, A. V., Paterson, G. A., Hawkins, L., et al. (2019). Analysis of an updated paleointensity database (Q_{PI}-PINT) for 65–200 Ma: Implications for the long-term history of dipole moment through the Mesozoic. *Journal of Geophysical Research: Solid Earth*, *124*, 9999–10022. https://doi.org/10.1029/2018JB017287

Lebedev, I. E., Tikhomirov, P. L., Pasenko, A. M., Eid, B., Lhuillier, F., & Pavlov, V. E. (2021). New paleomagnetic data on late Cretaceous Chukotka volcanics: The Chukotka block probably underwent displacements relative to the north American and Eurasian Plates after the formation of the Okhotsk–Chukotka Volcanic Belt? *Izvestiya, Physics of the Solid Earth*, *57*(2), 232–246. https://doi.org/10.1134/S1069351321020014

Levi, S. (1977). The effect of magnetite particle size on paleointensity determinations of the geomagnetic field. *Physics of the Earth and Planetary Interiors*, *13*, 245–259. https://doi.org/10.1016/0031-9201(77)90107-8

Lhuillier, F., Gilder, S. A., Wack, M., He, K., Petersen, N., Singer, B. S., et al. (2016). More stable yet bimodal geodynamo during the Cretaceous superchron? *Geophysical Research Letters*, *43*, 6170–6177. https://doi.org/10.1002/2016GL069303

Lhuillier, F., Shcherbakov, V. P., Gilder, S. A., & Hagstrum, J. T. (2017). Variability of the 0–3 Ma palaeomagnetic field observed from the boring volcanic field of the Pacific Northwest. *Geophysical Journal International*, *211*, 69–79. https://doi.org/10.1093/gji/ggx288

Lhuillier, F., Shcherbakov, V. P., Shcherbakova, V. V., Ostner, S., Hervé, G., & Petersen, N. (2019). Palaeointensities of Oligocene and Miocene volcanic sections from Ethiopia: Field behaviour during the Cainozoic. *Geophysical Journal International*, *216*, 1482–1494. https://doi.org/10.1093/gji/ggy491

Lowrie, W., & Kent, D. V. (2004). Geomagnetic polarity timescales and reversal frequency regimes. In J. E. T. Channell, D. V. Kent, W. Lowrie, & J. G. Meert (Eds.), *Timescales of the paleomagnetic field* (pp. 117–129). AGU.

McFadden, P. L., & Merrill, R. T. (1984). Lower mantle convection and geomagnetism. *Journal of Geophysical Research*, *89*(B5), 3354–3362. https://doi.org/10.1029/JB089iB05p03354

Muxworthy, A. R. (2010). Revisiting a domain-state independent method of palaeointensity determination. *Physics of the Earth and Planetary Interiors*, *179*, 21–31. https://doi.org/10.1016/j.pepi.2010.01.003

Nagata, T., Arai, Y., & Momose, K. (1963). Secular variation of the geomagnetic total force during the last 5000 years. *Journal of Geophysical Research*, *68*(18), 5277–5281. https://doi.org/10.1029/j.2156-2202.1963.tb00005.x

Nishitani, T., & Kono, M. (1983). Curie temperature and lattice constant of oxidized titanomagnetite. *Geophysical Journal of the Royal Astronomical Society*, *74*, 585–600. https://doi.org/10.1111/j.1365-246X.1983.tb01890.x

Ogg, J. G. (2020). Geomagnetic polarity time scale. In F. M. Gradstein, J. G. Ogg, M. D. Schmitz, & G. M. Ogg (Eds.), *Geologic time scale 2020* (pp. 159–192). https://doi.org/10.1016/b978-0-12-824360-2.00005-x

Paterson, G. A., Biggin, A. J., Hodgson, E., & Hill, M. J. (2015). Thellier-type paleointensity data from multidomain specimens. *Physics of the Earth and Planetary Interiors*, *245*, 117–133. https://doi.org/10.1016/j.pepi.2015.06.003

Paterson, G. A., Heslop, D., & Muxworthy, A. R. (2010). Deriving confidence in paleointensity estimates. *Geochemistry, Geophysics, Geosystems*, *11*, Q07Z18. https://doi.org/10.1029/2010GC003071

Paterson, G. A., Tauxe, L., Biggin, A. J., Shaar, R., & Jonestrask, L. C. (2014). On improving the selection of Thellier-type paleointensity data. *Geochemistry, Geophysics, Geosystems*, *15*, 1180–1192. https://doi.org/10.1002/2013GC005135

Pavlov, V. E., & Gallet, Y. (2005). A third superchron during the Early Paleozoic. *Episodes*, *28*(2), 78–84. https://doi.org/10.18814/epiiugs/2005/v28i2/001

Pavlov, V. E., & Gallet, Y. (2010). Variations in geomagnetic reversal frequency during the Earth's middle age. *Geochemistry, Geophysics, Geosystems*, *11*, Q01Z10. https://doi.org/10.1029/2009GC002583

Pick, T., & Tauxe, L. (1993). Geomagnetic palaeointensities during the Cretaceous Normal Superchron measured using submarine basaltic glass. *Nature*, *366*(6452), 238–242. https://doi.org/10.1038/366238a0

Prévot, M., Derder, M. E.-M., McWilliams, M., & Thompson, J. (1990). Intensity of the Earth's magnetic field: Evidence for a Mesozoic dipole low. *Earth and Planetary Science Letters*, *97*, 129–139. https://doi.org/10.1016/0012-821X(90)90104-6

Radhakrishna, T., Mohamed, A. R., Venkateshwarlu, M., & Soumya, G. S. (2020). Low geomagnetic field strength during End-Cretaceous Deccan volcanism and whole mantle convection. *Scientific Reports*, *10*(1), 10743. https://doi.org/10.1038/s41598-020-67245-6

Riisager, P., & Riisager, J. (2001). Detecting multidomain magnetic grains in Thellier palaeointensity experiments. *Physics of the Earth and Planetary Interiors*, *125*, 111–117. https://doi.org/10.1016/S0031-9201(01)00236-9

Ruiz, R. G., Goguitchaichvili, A., Geuna, S. E., Alva-Valdivia, L., Solé, J., & Morales, J. (2006). Early Cretaceous absolute geomagnetic paleointensities from Córdoba Province (Argentina). *Earth, Planets and Space*, *58*, 1333–1339. https://doi.org/10.1186/BF03352629

Selkin, P. A., & Tauxe, L. (2000). Long-term variations in palaeointensity. *Philosophical Transactions of the Royal Society of London, Series A*, *358*(1768), 1065–1088. https://doi.org/10.1098/rsta.2000.0574

Shcherbakov, V. P., Gribov, S. K., Lhuillier, F., Aphinogenova, N. A., & Tsel'movich, V. A. (2019). On the reliability of absolute palaeointensity determinations on basaltic rocks bearing a thermochemical remanence. *Journal of Geophysical Research: Solid Earth*, *117*, 7616–7632. https://doi.org/10.1029/2019JB017873

Shcherbakov, V. P., Khokhlov, A. V., & Sycheva, N. K. (2019). Analysis of the hypothesis of a Giant Gaussian process as a means for describing secular variations of the geomagnetic field vector. *Izvestiya, Physics of the Solid Earth*, *55*(1), 182–194. https://doi.org/10.1134/S1069351319010099

Shcherbakov, V. P., Lhuillier, F., & Sycheva, N. K. (2021). Exact analytical solutions for kinetic equations describing thermochemical remanence acquisition for single-domain grains: Implications for absolute paleointensity determinations. *Journal of Geophysical Research: Solid Earth*, *126*, e2020JB021536. https://doi.org/10.1029/2020JB021536

Shcherbakov, V. P., & Sycheva, N. K. (2006). On the variation in the geomagnetic dipole over the geological history of the Earth. *Izvestiya, Physics of the Solid Earth*, *42*(3), 201–206. https://doi.org/10.1134/S1069351306030037

Shcherbakov, V. P., & Sycheva, N. K. (2013). On the intensity of the geomagnetic field in the geological past. *Izvestiya, Physics of the Solid Earth*, *49*(5), 699–717. https://doi.org/10.1134/S1069351313040095

Shcherbakova, V. V., Bakhmutov, V. G., Shcherbakov, V. P., Zhidkov, G. V., & Shpyra, V. V. (2012). Palaeointensity and palaeomagnetic study of Cretaceous and Palaeocene rocks from Western Antarctica. *Geophysical Journal International*, *189*(1), 204–228. https://doi.org/10.1111/j.1365-246X.2012.05357.x

Shcherbakova, V. V., Biggin, A. J., Veselovskiy, R. V., Shatsillo, A. V., Hawkins, L., Shcherbakov, V. P., et al. (2017). Was the Devonian geomagnetic field dipolar or multipolar? Palaeointensity studies of Devonian igneous rocks from the Minusa Basin (Siberia) and the Kola Peninsula dykes, Russia. *Geophysical Journal International*, *209*(2), 1265–1286. https://doi.org/10.1093/gji/ggx085

Shcherbakova, V. V., Perrin, M., Shcherbakov, V. P., Pavlov, V. E., Ayvaz'yan, A., & Zhidkov, G. V. (2009). Rock magnetic and paleointensity results from Mesozoic baked contacts of Armenia. *Earth, Planets and Space*, *61*(1), 23–39. https://doi.org/10.1186/BF03352882

Shcherbakova, V. V., Shcherbakov, V. P., & Heider, F. (2000). Properties of partial thermoremanent magnetization in pseudosingle domain and multidomain magnetite grains. *Journal of Geophysical Research*, *105*(B1), 767–781. https://doi.org/10.1029/1999JB900235

Shcherbakova, V. V., Shcherbakov, V. P., Zhidkov, G. V., & Lubnina, N. V. (2014). Palaeointensity determinations on rocks from Palaeoproterozoic dykes from the Kaapvaal Craton (South Africa). *Geophysical Journal International*, *197*(3), 1371–1381. https://doi.org/10.1093/gji/ggu098

Shcherbakova, V. V., Zhidkov, G. V., Shcherbakov, V. P., Latyshev, A. V., & Fetisova, A. M. (2015). Verifying the Mesozoic dipole low hypothesis by the Siberian trap data. *Izvestiya, Physics of the Solid Earth*, *51*(3), 362–382. https://doi.org/10.1134/s1069351315030155

Smirnov, A. V., Kulakov, E. V., Foucher, M. S., & Bristol, K. E. (2017). Intrinsic paleointensity bias and the long-term history of the geodynamo. *Science Advances*, *3*(2), e1602306. https://doi.org/10.1126/sciadv.1602306

Tanaka, H., & Yamamoto, Y. (2016). Palaeointensities from Pliocene lava sequences in Iceland: Emphasis on the problem of Arai plot with two linear segments. *Geophysical Journal International*, *205*(2), 694–714. https://doi.org/10.1093/gji/ggw031

Tarduno, J. A., Cottrell, R. D., & Smirnov, A. V. (2001). High geomagnetic intensity during the Mid-Cretaceous from Thellier analyses of single plagioclase crystals. *Science*, *291*(5509), 1779–1783. https://doi.org/10.1126/science.1057519

Tarduno, J. A., Cottrell, R. D., & Smirnov, A. V. (2002). The Cretaceous superchron geodynamo: Observations near the tangent cylinder. *Proceedings of the National academy of Sciences of the United States of America*, *99*(22), 14020–14025. https://doi.org/10.1073/pnas.222373499

Tauxe, L. (2006). Long-term trends in paleointensity: The contribution of DSDP/ODP submarine basaltic glass collections. *Physics of the Earth and Planetary Interiors*, *156*, 223–241. https://doi.org/10.1016/j.pepi.2005.03.022

Tauxe, L., Gee, J. S., Steiner, M. B., & Staudigel, H. (2013). Paleointensity results from the Jurassic: New constraints from submarine basaltic glasses of ODP Site 801C. *Geochemistry, Geophysics, Geosystems*, *14*, 4718–4733. https://doi.org/10.1002/ggge.20282

Tauxe, L., & Staudigel, H. (2004). Strength of the geomagnetic field in the Cretaceous Normal Superchron: New data from submarine basaltic glass of the Troodos Ophiolite. *Geochemistry, Geophysics, Geosystems*, *5*, Q02H06. https://doi.org/10.1029/2003GC000635

Tauxe, L., & Yamazaki, T. (2015). Paleointensities. In M. Kono (Ed.), *Geomagnetism* (pp. 461–509). Elsevier. https://doi.org/10.1016/b978-0-444-53802-4.00107-x

Thellier, E., & Thellier, O. (1959). Sur l'intensité du champ magnétique terrestre dans le passé historique et géologique. *Annales de Géophysique*, *15*(3), 285–376.

Tikhomirov, P. L., Kalinina, E. A., Moriguti, T., Makishima, A., Kobayashi, K., Cherepanova, I. Y., et al. (2012). The Cretaceous Okhotsk–Chukotka Volcanic Belt (NE Russia): Geology, geochronology, magma output rates, and implications on the genesis of silicic LIPs. *Journal of Volcanology and Geothermal Research*, *221–222*, 14–32. https://doi.org/10.1016/j.jvolgeores.2011.12.011

Tikhomirov, P. L., Lebedev, I. E., Lhuillier, F., & Pavlov, V. (2021). Stratigraphy of the Okhotsk–Chukotka belt (headwaters of Malyi Anyui River, the vicinity of Kupol deposit): U–Pb and ^{40}Ar/^{39}Ar age data. *Doklady Earth Sciences*, *501*(2), 1059–1064. https://doi.org/10.1134/S1028334X2112014X

Tsunakawa, H., Wakabayashi, K.-i., Mochizuki, N., Yamamoto, Y., Ishizaka, K., Hirata, T., et al. (2009). Paleointensity study of the middle Cretaceous Iritono granite in northeast Japan: Implication for high field intensity of the Cretaceous Normal Superchron. *Physics of the Earth and Planetary Interiors*, *176*(3–4), 235–242. https://doi.org/10.1016/j.pepi.2009.07.001

Valet, J.-P. (2003). Time variations in geomagnetic intensity. *Reviews of Geophysics*, *41*(1), 1004. https://doi.org/10.1029/2001RG000104

Valet, J.-P., Meynadier, L., & Guyodo, Y. (2005). Geomagnetic dipole strength and reversal rate over the past two million years. *Nature*, *435*(7043), 802–805. https://doi.org/10.1038/nature03674

Wilson, R. L. (1961). The thermal demagnetization of natural magnetic moments in rocks. *Geophysical Journal International*, *5*(1), 45–58. https://doi.org/10.1111/j.1365-246X.1961.tb02928.x

Zhao, X., Liu, Q., Paterson, G. A., Qin, H., Cai, S., Yu, Y., et al. (2014). The effects of secondary mineral formation on Coe-type paleointensity determinations: Theory and simulation. *Geochemistry, Geophysics, Geosystems*, *15*, 1215–1234. https://doi.org/10.1002/2013GC005165

Zhu, R., Pan, Y., He, H., Qin, H., & Ren, S. (2008). Palaeomagnetism and ^{40}Ar/^{39}Ar age from a Cretaceous volcanic sequence, Inner Mongolia, China: Implications for the field variation during the Cretaceous Normal Superchron. *Physics of the Earth and Planetary Interiors*, *169*, 59–75. https://doi.org/10.1016/j.pepi.2008.07.025

Ziegler, L. B., Constable, C. G., Johnson, C. L., & Tauxe, L. (2011). PADM2M: A penalized maximum likelihood model of the 0–2 Ma palaeomagnetic axial dipole moment. *Geophysical Journal International*, *184*, 1069–1089. https://doi.org/10.1111/j.1365-246X.2010.04905.x

Zijderveld, J. D. A. (1967). A.C. Demagnetization of rocks: Analysis of results. In D. Collinson, K. M. Creer, & S. K. Runcorn (Eds.), *Methods in paleomagnetism* (pp. 254–286). Elsevier.